







Energy gap of topological surface states in proximity to a magnetic insulator

Jiashu Wang ^{1✉}, Tianyi Wang¹, Mykhaylo Ozerov², Zhan Zhang³, Joaquin Bermejo-Ortiz⁴, Seul-Ki Bac ¹, Hoai Trinh¹, Maksym Zhukovskiy⁵, Tatyana Orlova⁵, Haile Ambaye⁶, Jong Keum ^{6,7}, Louis-Anne de Vaultchier⁴, Yves Guldner⁴, Dmitry Smirnov², Valeria Lauter ⁶, Xinyu Liu ¹ & Badih A. Assaf ^{1✉}

Topological surface-states can acquire an energy gap when time-reversal symmetry is broken by interfacing with a magnetic insulator. This gap has yet to be measured. Such topological-magnetic insulator heterostructures can host a quantized anomalous Hall effect and can allow the control of the magnetic state of the insulator in a spintronic device. In this work, we observe the energy gap of topological surface-states in proximity to a magnetic insulator using magneto-optical Landau level spectroscopy. We measure $\text{Pb}_{1-x}\text{Sn}_x\text{Se-EuSe}$ heterostructures grown by molecular beam epitaxy exhibiting a record mobility and low Fermi energy. Through temperature dependent measurements and theoretical calculations, we show this gap is likely due to quantum confinement and conclude that the magnetic proximity effect is weak in this system. This weakness is disadvantageous for the realization of the quantum anomalous Hall effect, but favorable for spintronic devices which require the preservation of spin-momentum locking at the Fermi level.

¹Department of Physics and Astronomy, University of Notre Dame, Notre Dame, IN, USA. ²National High Magnetic Fields Laboratory, Florida State University, Tallahassee, FL, USA. ³X-ray Science Division, Advanced Photon Source, Argonne National Lab, Lemont, IL, USA. ⁴Laboratoire de Physique de l'École normale supérieure, ENS, Université PSL, CNRS, Sorbonne Université, Paris, France. ⁵Notre Dame Integrated Imaging Facility, University of Notre Dame, Notre Dame, IN, USA. ⁶Neutron Scattering Division, Neutron Sciences Directorate, Oak Ridge National Laboratory, Oak Ridge, TN, USA. ⁷Center for Nanophase Materials Sciences, Physical Science Directorate, Oak Ridge National Laboratory, Oak Ridge, TN, USA. ✉email: jwang39@nd.edu; bassaf@nd.edu

Topological insulators are materials that host gapless Dirac surface states due to a band inversion at high symmetry points in momentum space^{1,2}. Charge carriers occupying these states have their spin degree of freedom locked to the momentum thus enabling spin-charge conversion. When these topological Dirac states are in proximity with magnetism, they acquire an energy gap due to broken time-reversal symmetry as illustrated in Fig. 1a^{1,3,4}. Topological insulator (TI)—magnetic insulator (MI) heterostructures are being pursued both for spintronic device applications^{5–9} and to realize new quantum effects with broken time-reversal symmetry. The study of these heterostructures has thus been a consistent topic of interest both for applications and fundamental physics.

Fundamentally, the magnetic proximity effect is a route to introduce magnetism onto various states of matter without chemical doping^{1,3,10–13}. It is being pursued in topological insulators for the realization of the quantized anomalous Hall effect (QAHE)¹⁰ which requires topological surface state to have a large energy gap. In topological crystalline insulators (TCIs) which are topological materials with valley degenerate surface states protected by mirror symmetry, the QAHE effect has not yet been achieved. It is predicted to be large and tunable, owing to the valley degeneracy of TCIs enhancing the Chern number¹⁴.

Several experiments have studied the electrical and magnetic properties of heterostructures of a topological and a magnetic insulator, but the electronic structure and energy gap of topological surface states in proximity with magnetism have yet to be measured^{3,15–22}. A knowledge of the size of this gap is important as it provides a metric of the strength of the magnetic proximity effect. The exact nature of spin-momentum locking in the presence of time reversal symmetry breaking also depends on the size of this energy gap^{23,24}. Its measurement in the presence of a magnetic proximity with an insulator is thus important for spintronic devices. This measurement has not yet been done partly because most tools utilized to probe band structure are surface sensitive and cannot probe states located below a nanometer-thick MI layer. We will refer to states located at the TI/MI interface as topological interface states (TIS) in the remainder of this work. The mechanism by which the MI interacts with an underlying TIS remains unclear and controversial^{25,26}. A measurement of the energy gap of the TIS can also shed light on this problem.

Here, we report a measurement of this energy gap E_{TIS} when the TIS of a topological crystalline insulator are in proximity to an MI. The measurements are carried out using magneto-optical Landau level spectroscopy on $\text{Pb}_{1-x}\text{Sn}_x\text{Se}$ -EuSe heterostructures grown by molecular beam epitaxy (MBE) and sketched in Fig. 1b. We find $E_{\text{TIS}} = 14 \pm 6$ meV when the topological states are in proximity with magnetism. Polarized neutron reflectometry (PNR) and SQUID magnetometry measurements demonstrate that the alternating EuSe layers are in a fully saturated ferromagnetic state in proximity to the TIS at low temperature and high magnetic field. The origin of E_{TIS} in our experiment is shown to be mainly due to quantum confinement, while magnetism and time-reversal symmetry breaking play a minor role despite the presence of the magnetic EuSe layer. Our work thus establishes a previously unknown upper limit on the TIS gap due to the magnetic proximity effect. Importantly, we find that in $\text{Pb}_{1-x}\text{Sn}_x\text{Se}$ -EuSe, the Fermi energy is only 40 meV above the middle of E_{TIS} demonstrating the potential of topological crystalline insulators as high-quality alternatives for the realization of TI-MI devices.

Our material of choice $\text{Pb}_{1-x}\text{Sn}_x\text{Se}$ is a tunable topological crystalline insulator with degenerate surface states that are protected by mirror symmetry and time reversal symmetry^{14,27–30}. It is ideal to test the proximity effect since it has a crystal structure identical to Eu-chalcogenides, commonly used in magnetic proximity effect devices^{3,31}. Thus, it can be epitaxially matched to them without impacting sample quality^{32–34}. This fact allows the proximity-induced gap of the TIS to be measured using Landau level spectroscopy. This method is a highly reliable tool for measuring narrow energy gaps^{35–38} and for characterizing semimetals^{39–41}. The $\text{Pb}_{1-x}\text{Sn}_x\text{Se}$ -EuSe interface and our heterostructures also host a quasi-type-I band alignment with a band inversion and ensures that inversion symmetry is preserved. EuSe is however an antiferromagnet at zero field. But, by applying a large enough magnetic field along the growth axis of the heterostructure, needed for Landau level spectroscopy, we can saturate the magnetic moment of EuSe to a ferromagnetic state. In the configuration of our experiment, EuSe thus mimics a ferromagnetic insulator with a magnetization oriented out-of-plane.

Results

Structural properties of the heterostructures. The $\text{Pb}_{1-x}\text{Sn}_x\text{Se}$ /EuSe superlattices oriented in the (111) direction are grown on

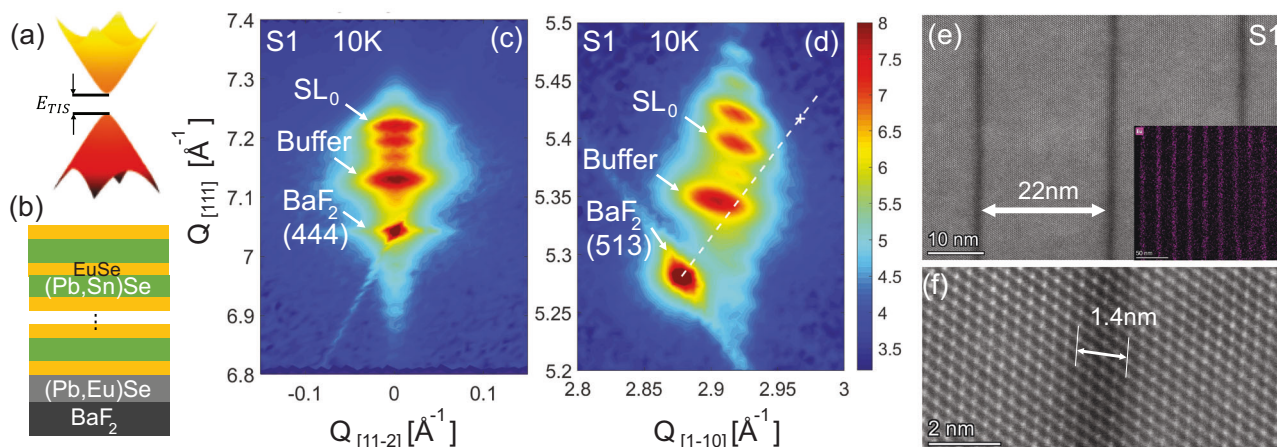


Fig. 1 Crystal structure of sample S1. **a** Sketch of the massive Dirac dispersion of topological interface states after gap opening. **b** Diagram of the sample structure. The EuSe/ $\text{Pb}_{1-x}\text{Sn}_x\text{Se}$ /EuSe structure is repeated 5 or 10 times. **c** Reciprocal space map (RSM) taken on sample S1 showing the (444) Bragg peak of the BaF_2 substrate, the $\text{Pb}_{1-x}\text{Eu}_x\text{Se}$ buffer layer and the $\text{Pb}_{1-x}\text{Sn}_x\text{Se}$ /EuSe superlattice (SL). **d** Reciprocal space map of the (513) Bragg reflection taken on S1. RSMs are taken at $T = 10$ K. The scale bar quantifies the intensity on a logarithmic scale. **e** Transmission electron microscopy image of a few wells from sample S1. Bottom right inset: Energy dispersive X-ray (EDX) spectroscopy map of the Eu distribution taken across all 10 periods of sample S1. **f** Zoom-in at the interface between $\text{Pb}_{1-x}\text{Sn}_x\text{Se}$ (light) and the EuSe barrier (dark).

Table 1 Sample list.

Sample	Sn concentration x	Pb _{1-x} Sn _x Se well thickness (nm)	EuSe barrier thickness (nm)	No. of periods
S1	0.28 ± 0.01 by EDX	22(±1)	1.41 ± 0.35 (4 ± 1 ML)	10
S2	0.25 ± 0.03 by EDX	25(±2)	2.4	5
S3	0.14 by XRD	32	6	5
N1	0.10 by XRD	48	11	5
N2	0.22 by XRD	35	4 ± 2, varies by layer	5

The Sn concentration is determined using energy dispersive X-ray spectroscopy (EDX) performed during transmission electron microscopy (TEM) and X-ray diffraction (XRD) on bulk control samples. The well and barrier thickness are extracted from a period determined by XRD of the superlattice and cross-sectional TEM measurements. The uncertainty accounts for the interface roughness. XRD patterns for all samples are shown in Supplementary note 1. ML: monolayer.

BaF₂ (111) substrates by MBE. First, a thick buffer layer of insulating Pb_{0.84}Eu_{0.16}Se (400–500 nm) is grown to reduce the lattice mismatch between the Pb_{1-x}Sn_xSe wells ($a = 6.107\text{--}6.088$ Å) and the substrate ($a = 6.196$ Å). Above the buffer layer we grow a periodic stack of Pb_{1-x}Sn_xSe/EuSe multiquantum wells. We study 5 samples listed in Table 1. Two samples N1 and N2 are dedicated to neutron reflectivity measurements. We focus on samples S1 and S2 in the manuscript.

X-ray diffraction (XRD) measurements carried out at $T = 10$ K, allow us to extract the strain state of S1 at temperatures of interest. In Fig. 1c, a reciprocal space map (RSM) taken along (444) at $T = 10$ K shows the Bragg peaks of the substrate, the (Pb,Eu)Se buffer layer and the Pb_{1-x}Sn_xSe well for sample S1. Periodic peaks from the superlattice structure are also resolved indicating a highly coherent heterostructure. The patterns allow us to extract the superlattice period for each sample. This is consistently checked with transmission electron microscopy (TEM) measurements and X-ray reflectometry (XRR) (see supplementary note 1) to extract the well and EuSe thickness separately. The structural properties of the samples are shown in Table 1. In Fig. 1d, an RSM along (513) allows us to compute the in-plane and out-of-plane lattice constant and extract information about the strain. The superlattice is under tensile strain ($\epsilon_{\parallel} \approx +0.4\%$) in the in-plane direction and compressive strain in the [111] direction.

Transmission electron microscopy images confirm the observations of XRD. Figure 1e shows a well-aligned stack of Pb_{1-x}Sn_xSe and EuSe probed using TEM in sample S1. The inset of this image displays an elemental mapping of the Eu atom using energy dispersive X-ray spectroscopy (EDX) that demonstrates the periodic repetition of the EuSe layers. A zoom-in figure (Fig. 1f) shows an interface between the well and the barrier demonstrating a short-range roughness of about a monolayer. We highlight that samples with thicker EuSe layers (>3 nm) yielded rougher interfaces, therefore we restrict this analysis to thinner layers. Additional XRD, XRR and TEM measurements are included in supplementary note 1. The large gap of EuSe (>1 eV) prohibits interactions between neighboring quantum wells, so the heterostructure can be safely considered as a multi-quantum well (see supplementary note 2)³⁴.

Magneto-optical measurements. We employ magneto-optical infrared spectroscopy to probe the energy gap of the TIS in proximity to EuSe. Experiments are performed in applied magnetic fields up to 17.5 T using both transmission and reflection measurements (Fig. 2a) and up to 35 T using absorption. The transmission spectra revealed a very weak signal between 25 and 72 meV corresponding to the reststrahlen band of the BaF₂ substrate. Therefore, we employed the reflection geometry to study the infrared signal from the heterostructure in this spectral range. In the presence of a magnetic field, infrared excites transitions between various Landau levels (LLs) as illustrated in

Fig. 2b. The minima in the normalized transmission spectra $T(B)/T(B=0)$ allow us to extract the energy of these transitions.

The experimental spectra obtained using transmission measurements are shown in Fig. 2c, d for S1. Owing to the high mobility of the TIS in Pb_{1-x}Sn_xSe, LL transitions that shift to higher energy as the field increases can be observed at fields as low as 3 T. Some are marked with blue and gray dots to highlight the field dependence. Color coding will become clear later.

To obtain information about the transitions occurring in the reststrahlen of the substrate, we carried out reflectivity measurements in the far-infrared. The relative reflectance is shown in Fig. 2e. Below 75 meV, reflectance is strong, and a prominent minimum marked with a black square is observed. Other field-independent modulations of the reflectivity are ignored, since they cannot be related to LLs and are of no interest for our analysis.

We identify all transitions observed as minima in Fig. 2c, d by points presented in Fig. 3a. Those transitions are shown in the empirical LL graphs plotted in Fig. 3b. By modeling these LL transitions using a massive Dirac Hamiltonian³² we can determine their origin. The transitions marked in blue in Fig. 2c, d and Fig. 3a are due to interband transitions between the conduction and valence LLs of the TIS. The intraband band transition between the 0th and the 1st LL is shown by the black square. Those marked in gray are associated with interband transitions from the LLs of trivial quantum well subbands. We make this attribution following analysis using the semi-empirical model discussed next.

Figure 3a shows a curve fit carried out using the following relation which describes interband magneto-optical transitions for massive Dirac fermions given dipole selection rules^{42,43} (see supplementary note 2):

$$\epsilon_n^{E,i} - \epsilon_{n\pm 1}^{H,i} = \sqrt{\Delta_i^2 + 2ev^2\hbar nB} + \sqrt{\Delta_i^2 + 2ev^2\hbar(n\pm 1)B}$$

Here Δ_i the band edge position of each subband, i is the subband index ($i = 1$ for the TIS), E/H denote the conduction and valence subbands respectively, v is the band velocity taken to be the same for all subbands, n is the Landau index, and B is the magnetic field. $\epsilon_n^{E,i}$ thus denotes the energy of the n^{th} LL of the i^{th} electron subband. A k.p formalism using the envelope function scheme allows us to derive the band dispersion to show that it indeed satisfies this quasi-ideal massive Dirac model (see supplementary notes 2 and 3)^{32,44}. The solid blue lines in Fig. 3a represent transitions obtained from Eq. (1) for the TIS and the gray lines represent those from trivial QW subbands. Their extrapolation to $B = 0$ yields the gap between each pair of conduction and valence subbands with the same index i (i.e. $2\Delta_i$ the gap between E_i and H_i). $2\Delta_1$ is E_{TIS} . It is zero for a thick quantum well and if time-reversal symmetry is preserved. The corresponding LLs for all subbands up to $i = 3$ are shown in Fig. 3b with the transitions shown as arrows.

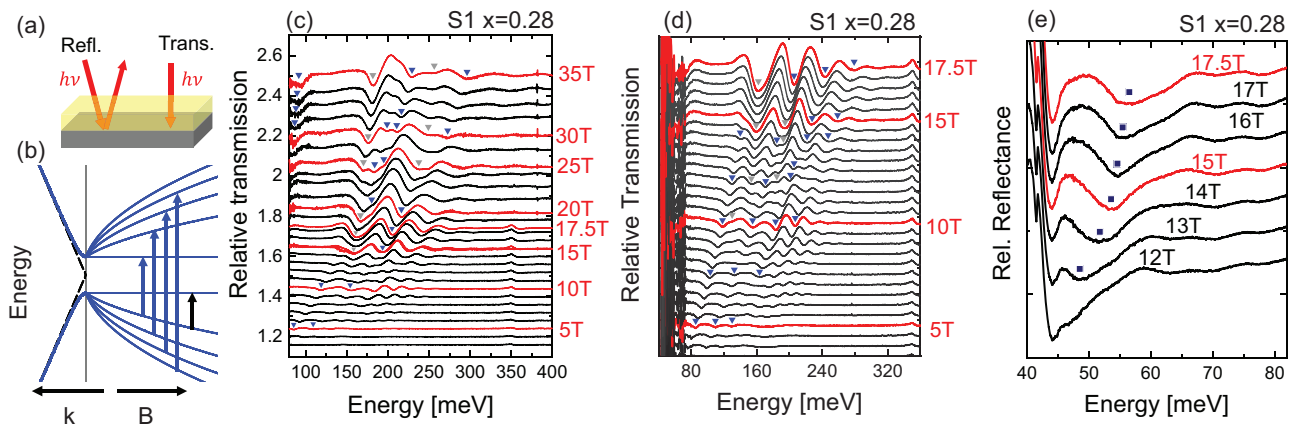


Fig. 2 Magneto-optical measurements taken on S1. Landau level (LL) spectroscopy setup in the **a** transmission and reflection geometry. Reflectance is carried out in the reststrahlen band of the substrate. **b** Band dispersion and LLs of gapped TIS versus wavenumber k and versus magnetic field B . Blue arrows represent interband Landau level transitions and the black arrow is the cyclotron resonance (CR). **c** Relative magneto-optical transmission spectra ($T(B)/T(0)$) measured between 3 T and 35 T on S1. **d** Zoom-in showing measurements taken between 3 and 17.5 T. **e** Relative reflectance spectra ($T(B)/T(0)$) measured between 12 T and 17.5 T on S1. All measurements are made at 4.5 K. The cyclotron resonance is marked with the black square, the structure of peaks and troughs near 40 meV is due to a BaF_2 phonon. The red curves highlight specific values of magnetic field for ease of reading.

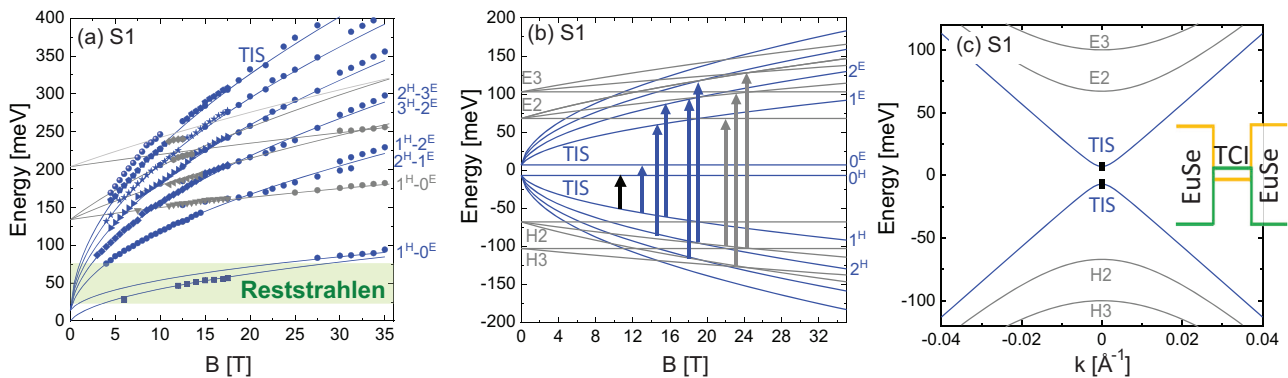


Fig. 3 Landau levels of sample S1 $\text{EuSe-Pb}_{0.72}\text{Sn}_{0.28}\text{Se-EuSe}$. **a** Fan chart extracted from the experimental measurements and compared to the empirical model. The solid lines are the calculated transitions. They follow the same color scheme. **b** Landau levels of $\text{Pb}_{0.72}\text{Sn}_{0.28}\text{Se-EuSe}$ utilized to compute the transitions shown in **a**. Blue points and arrows represent the interband transitions of the topological interface states (TIS), the gray points and arrows represent those of QW subbands E_i and H_i ($i > 2$) and the arrow represents the cyclotron resonance of the TIS. The numbers on the right ($n^{E/H}$) label the conduction and valence Landau levels of the TIS. **c** Band dispersion of $\text{Pb}_{0.72}\text{Sn}_{0.28}\text{Se-EuSe}$ obtained from the experiment. The uncertainty on the TIS energy gap is shown at the band edge. The inset shows the band alignment and the topological states peaked at the interface.

The cyclotron resonance (CR) corresponds to the intraband transition between the valence $n = 0$ and $n = 1$ levels of the TIS, whose energy is given by:

$$\epsilon_{CR} = \sqrt{\Delta_1^2 + 2ev^2\hbar nB} - \Delta_1$$

This transition is shown as the black line in Fig. 3a and the black arrow in Fig. 3b. The fit to the interband transitions and the CR in Fig. 3a yield the following gaps: the TIS gap $E_{TIS} = 2\Delta_1 = 14 \pm 6 \text{ meV}$, the gap between E_2 and H_2 $2\Delta_2 = 136 \pm 2 \text{ meV}$, and between E_3 and H_3 $2\Delta_2 = 206 \pm 2 \text{ meV}$. The Fermi energy can also be determined from to be 40 meV above the mid-gap from the field at which the 3-4 transition disappears as the $n = 3$ LL crosses the Fermi level (Fig. 3a, b). This experimental measurement allows us to reconstruct the band dispersion (in the QW plane) shown in Fig. 3c. Despite the presence of the EuSe layer, the TIS gap cannot exceed 20 meV within one standard deviation. The fit also yields the velocity $v = 4.3 \pm 0.05 \times 10^5 \text{ m/s}$ ($2.8 \text{ eV}\cdot\text{\AA}$) for both S1 and S2, in agreement with previous work^{32,45,46}. Since we observe several transitions between 3 T and 35 T, our uncertainty on v

and Δ_i is small. Data taken on sample S2 is presented in supplementary note 4 and yields similar but less precise results as its mobility was lower.

The experimental results for both samples S1 and S2 are shown in Table 2. The extracted energy gaps are compared to a theoretical calculation carried out to determine the impact of quantum confinement and strain on the trivial and topological states (supplementary notes 2 and 3). They utilize the band alignment shown in Fig. 3(c). The resulting gaps are also shown in Table 2. The TIS gap from the experiment is only slightly larger than the theoretical value calculated without including magnetic exchange. The calculated value after the inclusion of the impact of strain is within experimental error. Strain reduces the topological bulk gap of the $\text{Pb}_{0.72}\text{Sn}_{0.28}\text{Se}$, enhancing the hybridization between top and bottom TISs⁴⁷⁻⁴⁹. For this reason, it is found to enhance E_{TIS} . The experimental E_{TIS} is also equal within error to the confinement gap found in $\text{Pb}_{1-x}\text{Sn}_x\text{Se/EuSe}$ multiquantum wells in previous works³².

Temperature dependence. Additional temperature dependent magneto-optical spectroscopy measurements are carried out to

Table 2 Experimental and theoretical energy gaps for S1 and S2.

Sample ID	$E_{\text{TIS}} = 2\Delta_1$ (meV)	E2-H2 gap $2\Delta_2$	E3-H3 gap $2\Delta_3$
S1 - Exp.	14 ± 6	136(± 4) meV	206 meV
S1 - Cal.	7	129 meV	204 meV
S1 - Cal. with strain	10	122 meV	198 meV
S2 - Exp.	20 ± 10	118 ± 8 meV	200 meV
S2 - Calc.*	7 ± 4	116 meV	183 meV
S2 - Calc. with strain*	18 ± 6	106 meV	179 meV

The calculation utilizes an envelope function scheme implemented using the band alignment shown in the inset of Fig. 3c and discussed in the supplementary note 2. Magnetic exchange is neglected in these calculations. The measurements for S2 are shown in supplementary note 4. *For S2, the uncertainty on the calculated gap includes the uncertainty on the composition of the well from energy dispersive X-ray spectroscopy.

further corroborate the origin of the energy gap in S1. Spectra taken at various temperatures for $B = 13$ T are shown in Fig. 4a). The transition involving the $N = 1^{\text{H}}$ and $N = 2^{\text{E}}$ transition of the interface states is seen to vary in energy versus temperature, starting at 64 K. At 1.6, 4.2, and 6 K, the magneto-optical spectra are nearly-identical. The energy dependence at high temperatures is analyzed by fitting to the model discussed above, to extract E_{TIS} . The fan-charts shown in Fig. 4b–e demonstrate the changing energy gap, extracted by extrapolating the Landau levels to zero field using the massive Dirac model. Both E_{TIS} and $2\Delta_2$ are extracted and plotted in Fig. 4f. E_{TIS} is constant at the lowest temperatures 1.6 K to 6 K, where we expect the magnetic ordering transition of EuSe to take place. It increases between 64 K and 120 K. This increase can be fully understood as the result of the increasing penetration depth of surface states as a function of temperature³², caused by the decreasing bulk energy gap of $\text{Pb}_{1-x}\text{Sn}_x\text{Se}$ ^{37,50}. When this penetration depth increases, the hybridization between the top and bottom surfaces is enhanced and causes an enhanced gapping of their Dirac spectrum. These measurements suggest that the magnetic gap induced by proximity with EuSe is much smaller than the confinement gap at low temperatures.

Magnetic measurements. We have lastly performed SQUID magnetization measurements to identify the magnetic phases of our EuSe barriers. Figure 5a shows the magnetic moment versus temperature with $B = 100$ G applied parallel to the sample surface. The curve consists of two main contributions: the paramagnetic signal (PM) of the $\text{Pb}_{1-x}\text{Eu}_x\text{Se}$ buffer layer, which increases as the temperature decreases following the Curie law and the antiferromagnetic (AFM) signal from the EuSe barriers, which yields a peak at the Néel temperature. All curves shown in Fig. 5a exhibit such a peak, indicating AFM order from the EuSe barriers. The extracted Néel temperature T_{N} is plotted in Fig. 5b. It increases with Sn concentration. This is likely due to the strain caused by a change in the lattice parameter of the $\text{Pb}_{1-x}\text{Sn}_x\text{Se}$ layer with increasing x ⁵¹. The field-dependent magnetization was also measured and shown in Fig. 5c for the three samples considered here at 2 K. Based on the estimated thickness we have calculated the average magnetic moment \bar{m}_{Eu} per Eu^{2+} in Fig. 5c after the correction for diamagnetism of the BaF_2 substrate and the PM signal of the buffer layer (see supplementary note 5). The fine structure of the magnetization versus magnetic field—reflecting transitions from an AFM ground state to a ferrimagnetic phase and finally to a saturated state—is only visible for samples with a thick EuSe layer ($\geq 4\text{nm}$). But, the magnetic moment saturates to a value close to the expected saturation from Eu^{2+} ions,

$7\mu_{\text{B}}/\text{Eu}^{2+}$ ^{52,53}. Thus, for magnetic fields at which optical measurements are carried out, the moment of the EuSe layers can be considered saturated out-of-plane along the growth axis of the layer, and the extrapolation of the LLs to $B = 0$ should yield E_{TIS} in the presence of a ferromagnet in proximity.

To probe the depth profile of the magnetism at buried interfaces, we carried out PNR measurements on two samples (N1 and N2) at Oak Ridge National Lab. Data for N1 is shown in Fig. 5 and N2 is discussed in supplementary note 6. The PNR measurements yield the spin resolved reflectivities R_+ and R_- as a function of the wavevector transfer Q at a fixed magnetic field (Fig. 5d). Superscripts plus (or minus) denote measurements with neutrons with spin parallel (or antiparallel) to the direction of the applied magnetic field. The depth profiles of the nuclear and magnetic scattering length densities (NSLD and MSLD) correspond to the depth profile of the chemical and in-plane magnetization vector distributions, respectively. Both are extracted using the fit shown in Fig. 5d and plotted in Fig. 5e. Figure 5f shows the spin asymmetry ratio $SA = (R_+ - R_-)/(R_+ + R_-)$ obtained from the experimental and fitted curves at ± 4.85 T. The SA signal evidences the presence of a depth dependent magnetic moment. The simulated depth profile in Fig. 5e and the SA in Fig. 5f confirm that we successfully obtain the intended periodic repetition of magnetic layers in proximity to every $\text{Pb}_{1-x}\text{Sn}_x\text{Se}$ layer. The peak MSLD signal is nearly constant in each of the 7 layers and converts to a value close to $5.5\mu_{\text{B}}/\text{Eu}^{2+}$ slightly lower than the value recovered from magnetometry. Despite the interface being atomically sharp at the nm scale, some roughness can be resolved in TEM measurements at the μm scale. This can cause a slight reduction of the magnetic moment probed by PNR.

Discussion

We have thus extracted E_{TIS} for topological states in proximity to a magnetic insulator using Landau level spectroscopy. This is made possible by the synthesis of $\text{Pb}_{1-x}\text{Sn}_x\text{Se}$ -EuSe multiquantum wells that achieve record mobility close to $17000\text{cm}^2/\text{Vs}$ (see supplementary note 7). Using the known bulk band parameters of $\text{Pb}_{1-x}\text{Sn}_x\text{Se}$ with $x = 0.28$ ³⁷ and including the impact of quantum confinement and in-plane tensile strain on the energy levels (see supplementary note 3) we have reproduced the experimental energy gap without needing to include magnetic exchange interactions. The temperature dependence of E_{TIS} agrees with this assumption. The size of the magnetic exchange gap, is thus within the error bars shown in Figs. 3c and 4f. It is small and not conclusively detectable despite our detection of magnetic order at the interface. By comparing the top bound of our experimental gap from S1 to the theoretically computed gap, we can reliably set the upper bound of the magnetic gap to be 10 meV.

We highlight here that crystalline symmetry breaking, resulting from a lattice distortion has also been shown to gap the (001) topological surface states of TCIs in previous works, even in the absence of magnetism^{45,54,55}. However, the Dirac surface states at (111) surfaces have been found to be gapless by ARPES measurements down to low temperatures^{46,56}. The rhombic strain present in our layers, also should not break mirror symmetry at the (111) surface, also ruling out its role in generating a non-magnetic gap. Additionally, step edges in TCIs also on (001) surfaces have been shown to alter the electronic structure and to generate one-dimensional flat bands⁵⁷. Such effects cannot account for our recovered energy gap, they are however interesting to consider in future studies on the (001) surfaces of TCIs, even in the presence of magnetism. Lastly, roughness and interface modification was shown to impact the momentum space position and splitting of Dirac cones on the (001) surface⁵⁸.

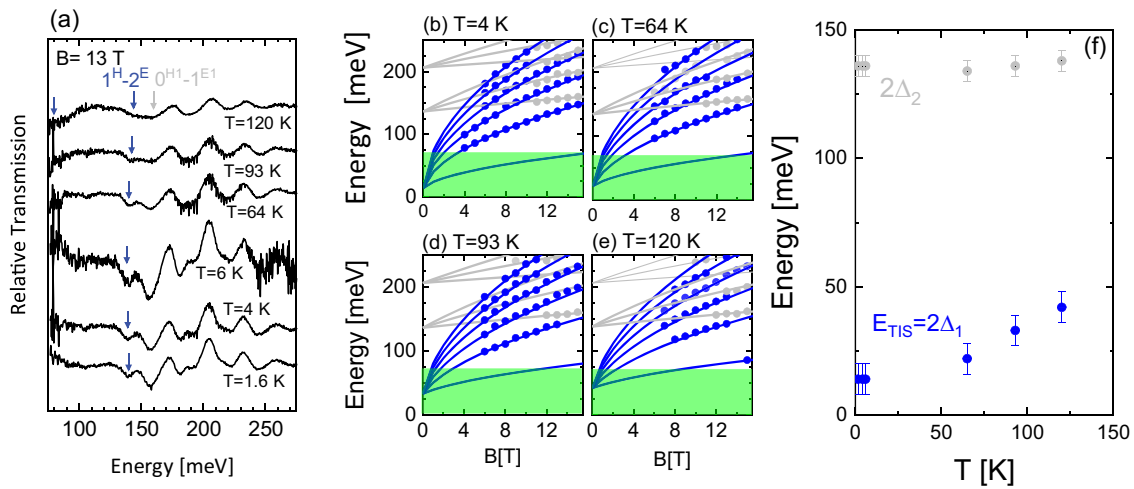


Fig. 4 Temperature dependent magneto-optical spectra of S1. **a** Magneto-optical spectra at $B = 13$ T measured on S1 at various temperatures. **b–e** Landau fan-charts extracted from the experimental measurements and compared to the empirical model. Blue points represent the interband transitions of the topological interface states (TIS), the gray points represent those of the first trivial quantum well state. Solid lines represent the calculated transitions. **f** The energy gap of the TIS (E_{TIS}) and the gap of the first quantum well subband ($2\Delta_2$) extracted from the temperature dependence analysis. The error bars in **f** present the uncertainty on the gap as a fit parameter from the curves shown in **b–e**.

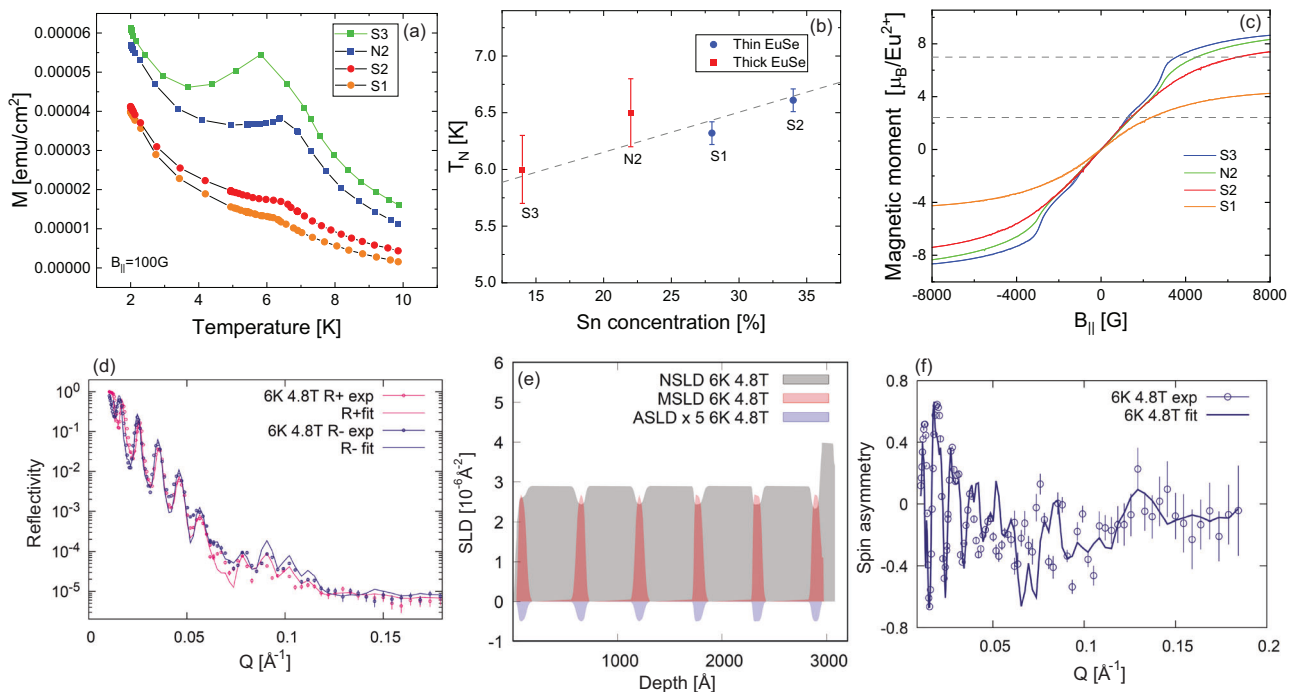


Fig. 5 Magnetic properties and polarized neutron reflectivity measurements. **a** Magnetization versus temperature at 0.01 T for 4 samples with different Sn concentrations. **b** The Neel temperature extracted from **(a)** for each sample plotted versus Sn concentration. **c** Magnetization versus magnetic field for samples with different Sn content. The dashed lines indicate the expected magnetic moment per Eu^{2+} in the ferrimagnetic and ferromagnetic states of EuSe . **d** Measured (symbols) and fitted (solid lines) neutron reflectivity curves for spin-up (R_+) and spin-down (R_-) neutron spin-states as a function of wavevector transfer $Q = 4\pi\sin(\theta)/\lambda$, where θ is the incident angle and λ is the neutron wavelength. **e** Polarized neutron reflectometry nuclear (NSLD, in gray), magnetic (MSLD, in pink) and absorption (ASLD, in blue) scattering length density profiles, measured 6 K with an external in-plane magnetic field of 4.5 T and presented as a function of depth. The finite ASLD is due to the presence of absorbing Eu atoms⁶⁸. **f** The spin asymmetry ratio, $SA = (R_+ - R_-)/(R_+ + R_-)$, obtained from the experimental and fitted reflectivity data in **d**.

While it has not been studied for the case of (111) surfaces, this findings should not influence our conclusion since the Dirac nodes on the (111) surface are pinned to specific symmetry points at $\bar{\Gamma}$ and \bar{M} , unlike those on the (001) surfaces, which occur along $\bar{\Gamma} - \bar{X}$ lines⁵⁶.

While the magnetic proximity induced gap of the TIS has never been measured, it has been computed for the $\text{Bi}_2\text{Se}_3/\text{EuS}$ interface.

Previous ab-initio simulations on this type of structure have yielded a small magnetic Dirac gap close to 3 meV for the interface, and 9 meV for the top surface⁴. The small gap obtained for the $\text{EuS-Bi}_2\text{Se}_3$ interface is associated to the highly localized nature of the f-orbital in Eu. At that interface, evidence of charge transfer was observed in experiments⁵⁹ and ab-initio calculations⁶⁰. In our system, charge transfer into the MI is unlikely since the two materials

should have a type-I band alignment and since the structure inherently preserves inversion symmetry. But, the scenario of orbital hybridization with the localized 4f-level could also hold which can explain our result that the proximity induced gap is small⁴. This allows us to draw an important conclusion. The magnetic proximity effect yields a narrow energy-gap at the interface between a TCI and rare earth containing insulators such as EuSe, which is not favorable for the realization of a stable QAHE. However, A narrow gap is advantageous for spintronic devices, since it is expected to preserve spin-momentum locking at the Fermi energy far-away from the band edges²³.

Methods

MBE synthesis. The heterostructures are grown by molecular beam epitaxy on BaF₂(111) substrates. A compounds source of PbSe is utilized along with elemental sources of the following elements: Sn, Se, and Eu. A thick buffer layer of (Pb,Eu)Se (400–500 nm) is initially grown to minimize dislocations in the heterostructures of interest. The buffer layer is followed by a EuSe/Pb_{1-x}Sn_xSe heterostructure with either 5 or 10 periods. The thickness of the well is denoted by d and that of the barrier by d_B . They are controlled by the growth time. Thickness of the EuSe barrier differs for each sample but is kept larger than or equal to 1.1 nm (3 ML). We chose to synthesize the Se-based TCIs for which Eu intermixing is known to be minimal⁶¹. The substrate temperature is fixed at 370 °C during the growth and the Sn content x is varied by adjusting the relative flux between the PbSe cell and a Sn cell. A constant Se over-pressure is maintained throughout the growth. The well composition in each case is determined either by growing a control bulk epilayer of Pb_{1-x}Sn_xSe (>200 nm) under the same conditions and during the same run as the heterostructures and extracting its composition using X-ray diffraction, or by carrying out energy dispersive X-ray spectroscopy.

Magneto-optical measurements. Magneto-infrared experiments were performed using a commercial FT-IR spectrometer coupled with the vertical bore superconducting magnet reaching 17.5 T and a resistive magnetic reaching 35 T at the National High Magnetic Fields Lab. The IR radiation propagates inside an evacuated metal tube from the spectrometer to the top of the magnet, whereas a brass light-pipe is used to guide the IR radiation down to the sample space. A parabolic cone was used to collect IR beam at the sample while two mirrors reflected the beam back up towards to the Si composite bolometer mounted just a short distance above the sample space. The sample is cooled down to 5 K using low pressure He exchange gas. The IR spectra were recorded in the mid-IR and far-IR range at fixed magnetic field, while field was stepped between 0 and 35 T with increment of 0.5 T. All measurements are carried out in the Faraday geometry with the incident beam propagating perpendicular to the surface and along the direction of the applied field. The reported spectra are obtained by dividing the signal at finite magnetic field by the zero-field spectrum.

Polarized neutron reflectometry. Polarized neutron reflectometry experiments were performed on the Magnetism Reflectometer at the Spallation Neutron Source at Oak Ridge National Laboratory⁶², using neutrons with wavelengths λ in a band of 2–8 Å and a high polarization of 98.5–99%. PNR is a highly penetrating depth-sensitive technique that can probe the chemical and magnetic depth profiles of materials with a resolution of 0.5 nm. The depth profiles of the nuclear and magnetic scattering length densities (NSLD and MSLD) correspond to the depth profile of the chemical and in-plane magnetization vector distributions, respectively^{63–67}. Measurements were conducted in a closed cycle refrigerator equipped with a 5 T cryomagnet. Using the time-of-flight method, a collimated polychromatic beam of polarized neutrons with the wavelength band $\Delta\lambda$ impinges on the film at a grazing angle θ , interacting with atomic nuclei and the spins of unpaired electrons. The reflected intensity R_+ and R_- are measured as a function of wave vector momentum, $Q = 4\pi\sin(\theta)/\lambda$, with the neutron spin parallel (+) or antiparallel (–) to the applied field. To separate the nuclear from the magnetic scattering, the spin asymmetry ratio $SA = (R_+ - R_-)/(R_+ + R_-)$ is calculated, for which $SA = 0$ designating no magnetic moment in the system.

X-ray diffraction. X-ray diffraction measurements are carried out at room temperature in a Bruker D8 Discover diffractometer equipped with Cu-K α -source. Low temperature X-ray diffraction measurements are carried out at beamline 33ID-D/E at the Advanced Photon Source at Argonne National lab using a wavelength of 0.61992 Å.

SQUID magnetometry. SQUID magnetometry is carried out in a Quantum Design MPMS, down to 4.2 K at various magnetic fields up to 7T. The field is applied parallel to the sample plane. The diamagnetism of the substrate measured at 2 K is subtracted from magnetization versus field measurements. The paramagnetism of the buffer layer is accounted for by a saturating Brillouin function and can be differentiated from the intrinsic magnetic properties of the EuSe layer using the method discussed in the supplementary note 5.

Transmission electron microscopy. High-resolution cross-sectional TEM images were acquired using a double tilt holder and probe corrected Spectra 30-300 transmission electron microscope (Thermo Fisher Scientific, USA) equipped with a field emission gun, operated at 300 kV. STEM images were acquired using Panther STEM detector (Thermo Fisher Scientific, USA) in high-angle, annular dark field mode (HAADF) and bright field mode (BF). For compositional analysis, energy-dispersive X-ray spectroscopy (EDX) maps were obtained in STEM mode using the Super-X EDX system (Thermo Fisher Scientific, USA) equipped with 4 windowless silicon drift detectors. TEM samples were prepared by focused ion beam etching using the standard lift-out technique.

Theoretical model. The band structure of the nontrivial Pb_{1-x}Sn_xSe heterostructures can be theoretically calculated using an envelope function model developed in previous work (for details see supplementary note 1)^{32,33}. The model does not take magnetism into account and has been shown to agree with experiments when the barrier is a simple insulator with a large energy gap (1 eV) without magnetic order³². The inverted band structure in the non-trivial Pb_{1-x}Sn_xSe will lead to a confined topological interface state (TIS). The bulk bands of the system also yield trivial quantum well subbands. The dispersion of these bands is calculated by an empirical 4-band massive Dirac model that includes a small parabolic correction:

$$\epsilon(k) = \pm \sqrt{\left(\Delta_i + \frac{\hbar^2 k^2}{2\tilde{m}}\right)^2 + \hbar^2 v^2 k^2}$$

Where Δ_i is the energy gap, v is the band velocity equal for the bulk and the confined system and k is the wavevector in the quantum well plane. The LLs of each band can be computed in a similar way:

$$\epsilon_{n,\uparrow}^{E/H}(B) = +\hbar\tilde{\omega} \pm \sqrt{(\Delta_i + \hbar n\tilde{\omega})^2 + 2e v^2 \hbar n B}$$

$$\epsilon_{n,\downarrow}^{E/H}(B) = -\hbar\tilde{\omega} \pm \sqrt{(\Delta_i + \hbar n\tilde{\omega})^2 + 2e v^2 \hbar n B}$$

$\tilde{\omega} = eB/\tilde{m}$ is the far-band correction to the effective mass \tilde{m} . It is generally yielding a massive Dirac model. The arrows indicate the pseudo-spin direction. E/H label the conduction and valence levels.

In the magneto-optical measurement in the Faraday geometry, the selection rules require that electrons can only transition from n^H (the n^H LL in valence band) to $(n \pm 1)^E$, and vice versa. Eq. (1) is derived with this in mind. More details concerning the model are given in supplementary note 2.

Data availability

The data that support the findings of this study are available from the corresponding author upon reasonable request.

Code availability

Code that supports the findings of this study is available from the corresponding author upon reasonable request.

Received: 2 January 2023; Accepted: 28 July 2023;

Published online: 05 August 2023

References

- Hasan, M. Z. & Kane, C. L. Colloquium: topological insulators. *Rev. Mod. Phys.* **82**, 3045–3067 (2010).
- Qi, X.-L. & Zhang, S.-C. Topological insulators and superconductors. *Rev. Mod. Phys.* **83**, 1057–1110 (2011).
- Wei, P. et al. Exchange-coupling-induced symmetry breaking in topological insulators. *Phys. Rev. Lett.* **110**, 186807 (2013).
- Lee, A. T., Han, M. J. & Park, K. Magnetic proximity effect and spin-orbital texture at the Bi₂Se₃/EuS interface. *Phys. Rev. B* **90**, 155103 (2014).
- Mellnik, A. R. et al. Spin-transfer torque generated by a topological insulator. *Nature* **511**, 449–451 (2014).
- Han, J. et al. Room-temperature spin-orbit torque switching induced by a topological insulator. *Phys. Rev. Lett.* **119**, 077702 (2017).
- Fanchiang, Y. T. et al. Strongly exchange-coupled and surface-state-modulated magnetization dynamics in Bi₂Se₃/yttrium iron garnet heterostructures. *Nat. Commun.* **9**, 223 (2018).
- Li, P. et al. Magnetization switching using topological surface states. *Sci. Adv.* **5**, eaaw3415 (2019).
- Rojas-Sánchez, J.-C. et al. Spin to charge conversion at room temperature by spin pumping into a new type of topological insulator: α -Sn films. *Phys. Rev. Lett.* **116**, 096602 (2016).

10. Tokura, Y., Yasuda, K. & Tsukazaki, A. Magnetic topological insulators. *Nat. Rev. Phys.* **1**, 126–143 (2019).
11. Norden, T. et al. Giant valley splitting in monolayer WS₂ by magnetic proximity effect. *Nat. Commun.* **10**, 4163 (2019).
12. Hauser, J. J. Magnetic proximity effect. *Phys. Rev.* **187**, 580–583 (1969).
13. Yao, X. et al. Record high-proximity-induced anomalous Hall effect in (BiSb_{1-x})₂Te₃ thin film grown on CrGeTe₃ substrate. *Nano Lett.* [acs.nanolett.9b01495](https://doi.org/10.1021/acs.nanolett.9b01495) <https://doi.org/10.1021/acs.nanolett.9b01495> (2019).
14. Fang, C., Gilbert, M. J. & Bernevig, B. A. Large- Chern-number quantum anomalous hall effect in thin-film topological crystalline insulators. *Phys. Rev. Lett.* **112**, 046801 (2014).
15. Katmis, F. et al. A high-temperature ferromagnetic topological insulating phase by proximity coupling. *Nature* **533**, 513–516 (2016).
16. Assaf, B. A. et al. Inducing magnetism onto the surface of a topological crystalline insulator. *Phys. Rev. B* **91**, 195310 (2015).
17. Kandala, A. et al. Growth and characterization of hybrid insulating ferromagnet-topological insulator heterostructure devices. *Appl. Phys. Lett.* **103**, 202409 (2013).
18. Yang, Q. I. et al. Emerging weak localization effects on a topological insulator-insulating ferromagnet (Bi₂Se₃-EuS) interface. *Phys. Rev. B* **88**, 081407 (2013).
19. Lang, M. et al. Proximity induced high-temperature magnetic order in topological insulator - ferrimagnetic insulator heterostructure. *Nano Lett.* **14**, 3459–3465 (2014).
20. Riddiford, L. J. et al. Understanding signatures of emergent magnetism in topological insulator/ferrite bilayers. *Phys. Rev. Lett.* **128**, 126802 (2022).
21. Grutter, A. J. & He, Q. L. Magnetic proximity effects in topological insulator heterostructures: Implementation and characterization. *Phys. Rev. Mater.* **5**, 090301 (2021).
22. He, Q. L. et al. Tailoring exchange couplings in magnetic topological-insulator/antiferromagnet heterostructures. *Nat. Mater.* **16**, 94–100 (2017).
23. Xu, S.-Y. et al. Hedgehog spin texture and Berry's phase tuning in a magnetic topological insulator. *Nat. Phys.* **8**, 616–622 (2012).
24. Lu, H.-Z., Zhao, A. & Shen, S.-Q. Quantum transport in magnetic topological insulator thin films. *Phys. Rev. Lett.* **111**, 146802 (2013).
25. Figueroa, A. I. et al. Absence of magnetic proximity effect at the interface of Bi₂Se₃ and (Bi,Sb)₂Te₃ with EuS. *Phys. Rev. Lett.* **125**, 226801 (2020).
26. Prokeš, K. et al. Search for enhanced magnetism at the interface between Bi₂Se₃ and EuSe. *Phys. Rev. B* **103**, 115438 (2021).
27. Hsieh, T. H. et al. Topological crystalline insulators in the SnTe material class. *Nat. Commun.* **3**, 982 (2012).
28. Hsieh, T. H. et al. Corrigendum: topological crystalline insulators in the SnTe material class. *Nat. Commun.* **4**, 1901 (2013).
29. Serbyn, M. & Fu, L. Symmetry breaking and Landau quantization in topological crystalline insulators. *Phys. Rev. B - Condens. Matter Mater. Phys.* **90**, 035402 (2014).
30. Ando, Y. & Fu, L. Topological crystalline insulators and topological superconductors: from concepts to materials. *Annu. Rev. Condens. Matter Phys.* **6**, 361–381 (2015).
31. Krieger, J. A. et al. Do topology and ferromagnetism cooperate at the EuS/Bi₂Se₃ interface? *Phys. Rev. B* **99**, 064423 (2019).
32. Krizman, G. et al. Tunable Dirac interface states in topological superlattices. *Phys. Rev. B* **98**, 075303 (2018).
33. Wang, J. et al. Weak antilocalization beyond the fully diffusive regime in Pb_{1-x}Sn_xSe topological quantum wells. *Phys. Rev. B* **102**, 155307 (2020).
34. Krizman, G. et al. Miniband engineering and topological phase transitions in topological-insulator-normal-insulator superlattices. *Phys. Rev. B* **103**, 235302 (2021).
35. Jiang, Y. et al. Unraveling the topological phase of ZrTe₅ via magnetoinfrared spectroscopy. *Phys. Rev. Lett.* **125**, 046403 (2020).
36. Jiang, Y. et al. Electron-hole asymmetry of surface states in topological insulator Sb₂Te₃ thin films revealed by magneto-infrared spectroscopy. *Nano Lett.* **20**, 4588–4593 (2020).
37. Krizman, G. et al. Dirac parameters and topological phase diagram of Pb_{1-x}Sn_xSe from magnetospectroscopy. *Phys. Rev. B* **98**, 245202 (2018).
38. Teppe, F. et al. Temperature-driven massless Kane fermions in HgCdTe crystals. *Nat. Commun.* **7**, 12576 (2016).
39. Yuan, X. et al. The discovery of dynamic chiral anomaly in a Weyl semimetal NbAs. *Nat. Commun.* **11**, 1259 (2020).
40. Shao, Y. et al. Electronic correlations in nodal-line semimetals. *Nat. Phys.* **16**, 636–641 (2020).
41. Krizman, G. et al. Determination of the crystal field splitting energy in Cd₃As₂ using magneto-optics. *Phys. Rev. B* **100**, 155205 (2019).
42. Bauer, G. Magneto-optical properties of IV–VI compounds. in *Narrow Gap Semiconductors Physics and Applications: Proceeding of the International Summer School* (ed. Zawadzki, W.) vol. 133 427–446 (Springer Berlin Heidelberg, 1980).
43. Mitchell, D. L. & Wallis, R. F. Theoretical energy-band parameters for the lead salts. *Phys. Rev.* **151**, 581–595 (1966).
44. Bastard, G. *Wave mechanics applied to semiconductor heterostructures*. Les editions de Physiques (1988).
45. Zeljkovic, I. et al. Dirac mass generation from crystal symmetry breaking on the surfaces of topological crystalline insulators. *Nat. Mater.* **14**, 318–324 (2015).
46. Mandal, P. S. et al. Topological quantum phase transition from mirror to time reversal symmetry protected topological insulator. *Nat. Commun.* **8**, 968 (2017).
47. Zaslavitskii, I. I., de Andrada e Silva, E. A., Abramof, E. & McCann, P. J. Optical deformation potentials for PbSe and PbTe. *Phys. Rev. B* **70**, 115302 (2004).
48. Simma, M., Fromherz, T., Bauer, G. & Springholz, G. Type I/type II band alignment transition in strained PbSe/PbEuSeTe multiquantum wells. *Appl. Phys. Lett.* **95**, 212103 (2009).
49. Simma, M., Bauer, G. & Springholz, G. Band alignments and strain effects in PbTe/Pb_{1-x}Sr_xTe and PbSe/Pb_{1-x}Sr_xSe quantum-well heterostructures. *Phys. Rev. B* **90**, 195310 (2014).
50. Wojek, B. M. et al. On the nature of the band inversion and the topological phase transition in (Pb,Sn)Se. *Phys. Rev. B* **90**, 161202 (2014).
51. Lechner, R. T. et al. Strain induced changes in the magnetic phase diagram of metamagnetic heteroepitaxial EuSe/PbSe_{1-x}Tex multilayers. *Phys. Rev. Lett.* **94**, 157201 (2005).
52. Wang, Y. et al. Epitaxial growth and magnetic characterization of EuSe thin films with various crystalline orientations. *J. Appl. Phys.* **131**, 055302 (2022).
53. Lechner, R. T. et al. Spin configurations in strained magnetic EuSe / PbSe_{1-x}Tex superlattices grown by molecular beam epitaxy. *Phys. E Low-Dimensional Syst. Nanostruct.* **32**, 379–382 (2006).
54. Okada, Y. et al. Observation of Dirac node formation and mass acquisition in a topological crystalline insulator. *Science* **341**, 1496–1499 (2013).
55. Wojek, B. M. et al. Direct observation and temperature control of the surface Dirac gap in a topological crystalline insulator. *Nat. Commun.* **6**, 8463 (2015).
56. Polley, C. M. et al. Observation of topological crystalline insulator surface states on (111)-oriented Pb_{1-x}Sn_xSe films. *Phys. Rev. B - Condens. Matter Mater. Phys.* **89**, 075317 (2014).
57. Sessi, P. et al. Robust spin-polarized midgap states at step edges of topological crystalline insulators. *Sci. (80-.)* **354**, 1269–1273 (2016).
58. Polley, C. M. et al. Fragility of the Dirac cone splitting in topological crystalline insulator heterostructures. *ACS Nano* **12**, 617–626 (2018).
59. Osterhoudt, G. B. et al. Charge transfer in heterostructures as indicated by the absence of Raman scattering. *Phys. Rev. B* **98**, 014308 (2018).
60. Tristant, D., Vekhter, I., Meunier, V. & Shelton, W. A. Partial charge transfer and absence of induced magnetization in EuS/Bi₂Se₃ heterostructures. *Phys. Rev. B* **104**, 075128 (2021).
61. Springholz, G. et al. Interdiffusion in Pb_{1-x}Eu_xSe/PbSe multi-quantum-well structures. *J. Cryst. Growth* **113**, 593–598 (1991).
62. Lauter, V., Ambaye, H., Goyette, R., Hal Lee, W. T. & Parizzi, A. Highlights from the magnetism reflectometer at the SNS. *Phys. B Condens. Matter* **404**, 2543–2546 (2009).
63. Lauter-Pasyuk, V. Neutron grazing incidence techniques for nano-science. *Collect. Soc. Fr. Neutron* **7**, s221–s240 (2007).
64. Blundell, S. J. et al. Spin-orientation dependence in neutron reflection from a single magnetic film. *Phys. Rev. B* **51**, 9395–9398 (1995).
65. Lauter-Pasyuk, V., Lauter, H. J., Toperverg, B. P., Romashev, L. & Ustinov, V. Transverse and lateral structure of the spin-flop phase in Fe/Cr antiferromagnetic superlattices. *Phys. Rev. Lett.* **89**, 167203 (2002).
66. Lauter, H. et al. Domains and interface roughness in Fe/Cr multilayers: influence on the GMR effect. *J. Magn. Magn. Mater.* **258–259**, 338–341 (2003).
67. Lauter-Pasyuk, V. et al. Magnetic off-specular neutron scattering from Fe/Cr multilayers. *Phys. B Condens. Matter* **283**, 194–198 (2000).
68. Korneev, D. A., Pasyuk, V. V., Petrenko, A. V. & Jankovskii, H. Absorbing sublayers and their influence on the polarizing efficiency of magnetic neutron mirrors. *Nucl. Instrum. Methods Phys. Res. Sect. B Beam Interact. Mater. At.* **63**, 328–332 (1992).

Acknowledgements

Work supported by NSF-DMR-1905277. A portion of this work was performed at the National High Magnetic Field Laboratory, which is supported by National Science Foundation Cooperative Agreements No. DMR-1644779, DMR-2128556, and the State of Florida. This research used resources at the Spallation Neutron Source, a Department of Energy Office of Science User Facility operated by the Oak Ridge National Laboratory. XRR measurements were conducted at the Center for Nanophase Materials Sciences (CNMS), which is a DOE Office of Science User Facility. We also acknowledge support from the Notre Dame Integrated Imaging Facility. This research used resources of the Advanced Photon Source, a U.S. Department of Energy (DOE) Office of Science User Facility, operated for the DOE Office of Science by Argonne National Laboratory under Contract No. DE-AC02-06CH11357.

Author contributions

J.W., X.L., and B.A.A. conceived the project. J.W., M.O., and S.K.B. carried out the magneto-optical experiments with input from B.A.A. and D.S. J.W., H.T., and S.K.B. analyzed the magneto-optical data. T.W. and J.W. carried out the k.p calculations. J.B.O., L.A.V., and Y.G. carried out temperature dependent magneto-optical measurements and analyzed them. J.W., Z.Z., and B.A.A. carried out X-ray diffraction measurements. M.Z. and T.O. carried out TEM measurements. V.L., H.A., and J.K. carried out and analyzed neutron reflectivity and X-ray reflectivity measurements. X.L. synthesized the samples. J.W., V.L., X.L., and B.A.A. interpreted the data from various experiments and wrote the manuscript.

Competing interests

The authors declare no competing interests.

Additional information

Supplementary information The online version contains supplementary material available at <https://doi.org/10.1038/s42005-023-01327-5>.

Correspondence and requests for materials should be addressed to Jiashu Wang or Badih A. Assaf.

Peer review information *Communications Physics* thanks the anonymous reviewers for their contribution to the peer review of this work.

Reprints and permission information is available at <http://www.nature.com/reprints>

Publisher's note Springer Nature remains neutral with regard to jurisdictional claims in published maps and institutional affiliations.



Open Access This article is licensed under a Creative Commons Attribution 4.0 International License, which permits use, sharing, adaptation, distribution and reproduction in any medium or format, as long as you give appropriate credit to the original author(s) and the source, provide a link to the Creative Commons license, and indicate if changes were made. The images or other third party material in this article are included in the article's Creative Commons license, unless indicated otherwise in a credit line to the material. If material is not included in the article's Creative Commons license and your intended use is not permitted by statutory regulation or exceeds the permitted use, you will need to obtain permission directly from the copyright holder. To view a copy of this license, visit <http://creativecommons.org/licenses/by/4.0/>.

© The Author(s) 2023